Interferometric synthetic aperture radar-GPS integration: Interseismic strain accumulation across the Hunter Mountain fault in the eastern California shear zone

Interferometric synthetic aperture radar–GPS integration: Interseismic strain accumulation across the Hunter Mountain fault in the eastern California shear zone

Noel Gourmelen,[1,2] Falk Amelung,[1] and Riccardo Lanari[3]

Received 20 October 2009; revised 24 April 2010; accepted 4 May 2010; published 28 September 2010.

[1] The principal limitations of interferometric synthetic aperture radar (InSAR) to measure subtle, long-wavelength deformation are uncertainties associated with the satellite orbits. We propose a method to remove orbital phase errors from the InSAR data by integrating InSAR and continuous GPS time series. We model the along-track variation of the baseline errors as second-order polynomials and estimate the coefficients using the continuous GPS measurements. We apply this method to a 600 km long region encompassing the Basin and Range and the eastern California shear zone. Comparison of the corrected InSAR velocities with independent GPS data shows that this method removes the long-wavelength InSAR errors. The InSAR data reveal a region of sharp variation in the line-of-sight velocity across the Hunter Mountain fault. We model the deformation as interseismic elastic strain accumulation across a strike-slip fault. The modeling suggests a fault slip rate of 4.9 ± 0.8 mm/yr and a locking depth of 2 ± 0.4 km. The shallow locking depth suggests that the Hunter Mountain fault is a transfer fault between low angle normal faults in the area.

Citation: Gourmelen, N., F. Amelung, and R. Lanari (2010), Interferometric synthetic aperture radar–GPS integration: Interseismic strain accumulation across the Hunter Mountain fault in the eastern California shear zone, *J. Geophys. Res.*, *115*, B09408, doi:10.1029/2009JB007064.

1. Introduction

[2] Interferometric synthetic aperture radar (InSAR) has been used successfully to measure and study surface deformation due to several phenomena such as glacier movements [*Goldstein et al.*, 1993], earthquakes [*Massonnet et al.*, 1994], and volcano inflation [*Amelung et al.*, 2000]. The measurement of subtle, long-wavelength deformation (>50 km), such as interseismic and postseismic deformation [*Massonnet*, 1997; *Pollitz et al.*, 2000], remains a challenge. The precision of the InSAR measurement is affected by decorrelation phenomena, phase contributions due to atmospheric water vapor and ionospheric effects, and uncertainties in the position of the satellites. The uncertainties in the position of the satellites (orbital errors) degrade the precision of the measurements from millimeters (the instrumental precision) to centimeters or more for long-wavelength deformation; the orbital errors cause relative line-of-sight (LOS) displacements over tens to hundreds of kilometers in the interferograms (referred to in this paper as orbital phase errors) that are difficult to separate from LOS displacements caused by interseismic strain accumulation. Precise orbits, such as the ones provided by the Delft Institute for Earth-Oriented Space Research (DEOS), have a standard deviation on the order of 15 cm [*Scharroo*, 2002], which translate into several centimeters of LOS displacements.

[3] Since the end of the 1990s, techniques for the simultaneous analysis of large numbers of SAR acquisitions (there are more than 150 acquisitions for most of Europe and 50–100 acquisition for other parts of the worlds) have led to time-dependent measurements [*Ferretti et al.*, 2001; *Berardino et al.*, 2002; *Lanari et al.*, 2004; *Hooper et al.*, 2004; *Casu et al.*, 2008]. These time series techniques, often referred to as persistent scatterers (PS) and small baseline subset (SBAS) approaches, have significantly improved measurement precision. In these algorithms, only those pixels remaining coherent in all or part of the interferograms are exploited; they are detected (and subsequently analyzed) by carrying statistical [*Ferretti et al.*, 2005] or coherence [*Berardino et al.*, 2002] analyses on a large SAR data set. The atmospheric phase contributions or atmospheric phase screen (APS) can be extracted and removed by applying spatial-temporal filtering on the time series [*Ferretti et al.*, 2001; *Berardino et al.*, 2002].

[4] Large-scale tectonic processes, such as interseismic deformation across entire fault zones and postseismic deformation following large earthquakes, can be studied using multiple, consecutive radar frames [*Peltzer et al.*, 2001;

[1]School of Marine and Atmospheric Science, University of Miami, Miami, Florida, USA.
[2]Now at School of Earth and Environment, University of Leeds, Leeds, UK.
[3]Istituto per il Rilevamento Elettromagnetico dell'Ambiente, CNR, Napoli, Italy.

0148-0227/10/2009JB007064

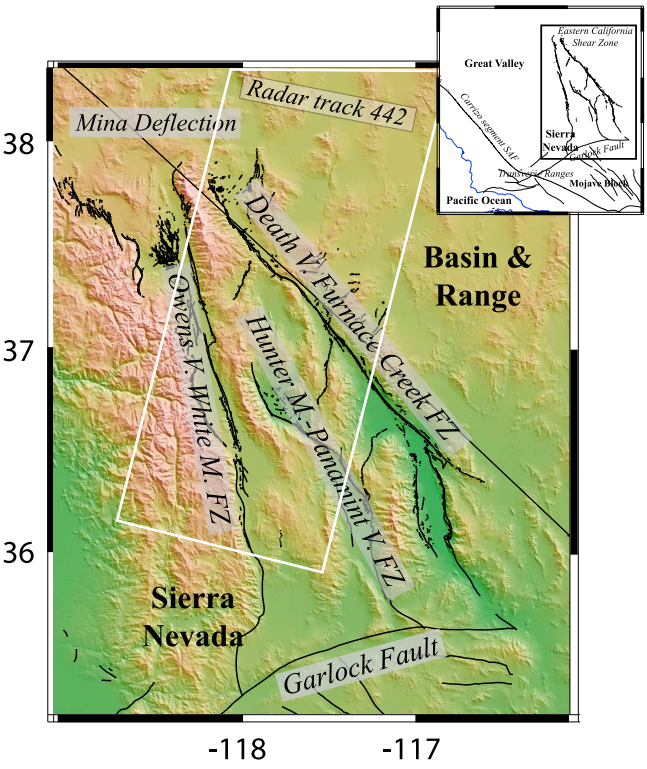

Figure 1. Major faults of the eastern California shear zone south of the Mina deflection and north of the Garlock fault. Location of the InSAR footprint across the ECSZ (white outline).

Wright et al., 2004; *Fialko*, 2006; *Biggs et al.*, 2007]. In this case, the measurement precision is limited mainly by long-wavelength phase contributions related to orbital errors (we refer to them as orbital phase errors). *Burgmann et al.* [2006] estimate a gradient of velocity error of 0.094 mm/yr/km from measuring residuals between CGPS and PS-InSAR velocity map. This gradient equates to 1 cm/yr over a 100 km distance, well in the range of many strike-slip faults.

[5] Subtle, long-wavelength deformation can be resolved using a priori information about the surface displacement field. For example, *Peltzer et al.* [2001] calibrate InSAR data across the eastern California shear zone using a model of long-term plate motion. *Fialko* [2006] uses more than 50 GPS velocities to remove a linear ramp from a stack of interferograms for the southern San Andreas fault. *Burgmann et al.* [2006], working in the San Francisco Bay Area, use a GPS-constrained tectonic model to remove a ramp from the InSAR velocities obtained using persistent scatterer methods.

[6] Various methods have been used to account for orbital phase errors. If a priori information about the displacement field is not available, long-wavelength deformation can be retrieved by simultaneous inversion for models for the tectonic deformation and for the orbital phase errors [*Wright et al.*, 2004; *Biggs et al.*, 2007]. In most studies, the orbital phase errors are approximated by a first-order or second-order two-dimensional polynomial. The ROI_PAC software package from the Jet Propulsion Laboratory [*Rosen et al.*, 2004] uses a realistic orbital model and topographic information to estimate the orbital phase errors. *Kohlhase et al.* [2003] remove the orbital phase errors using an orbital model and a network of SAR data. *Kohlhase et al.* [2003] and *Biggs et al.* [2007] use a network approach to resolve the orbital phase errors. This approach potentially retains the temporal resolution of the InSAR data, although Biggs et al. assume a linear deformation model.

[7] The limitations of the described methods are one or more of the following: (1) they do not account for deformation [*Kohlhase et al.*, 2003]; (2) they make assumptions about the spatial variation of the deformation [*Wright et al.*, 2004; *Biggs et al.*, 2007]; (3) they make assumptions about the time dependency of the deformation (usually assume linear deformation) [*Wright et al.*, 2004]; and (4) they use approximate orbital models [*Wright et al.*, 2004; *Biggs et al.*, 2007].

[8] In this paper, we present a new method for the measurement of subtle, long-wavelength deformation. The method identifies and removes orbital phase errors from the InSAR deformation time series by using GPS and a physical orbital model, without making assumptions about the displacement field in space and time. We apply this method to the eastern California shear zone, with particular emphasis on the Hunter Mountain fault zone.

2. The Eastern California Shear Zone

[9] The eastern California shear zone (ECSZ), parallel to the San Andreas fault system, accommodates 20%–25% of the total Pacific–North American plate motion [*Dokka and Travis*, 1990b, 1990a; *Dixon et al.*, 2000a] (Figure 1). During the past 150 years, four major earthquakes have hit the region: the 1872 M8 Owens Valley, the 1932 M7.1 Cedar Mountain, the 1992 M7.3 Landers, and the 1999 M7.1 Hector Mine Earthquakes. The Hunter Mountain fault is part of the Panamint Valley–Hunter Mountain–Saline Valley (PHS) system, one of the younger faults comprising the ECSZ north of the Garlock fault [*Lee et al.*, 2009]. The age of fault initiation is bracketed between 2.8 and 4.0 Ma [*Lee et al.*, 2009; *Burchfiel et al.*, 1987; *Hodges et al.*, 1989]. The total offset of the Hunter Mountain fault is estimated at 9.3 ± 1.4 km [*Burchfiel et al.*, 1987; *Sternloff*, 1988] based on the intersection of the Hunter Mountain batholith and the nearly horizontal unconformity at the base of Miocene-Pliocene volcanics; displacement of this feature across the Hunter Mountain fault is mainly horizontal, consistent with strike-slip motion. Published slip rates for the Hunter Mountain–Panamint Valley fault system range between 2.4 and 4 mm/yr [*Zhang et al.*, 1990; *Oswald and Wesnousky*, 2002; *Dixon et al.*, 2003].

3. Integration of InSAR Time Series With CGPS Measurements: Theory

3.1. Differential Interferometry

[10] Differential SAR interferometry (InSAR) is a remote sensing technique that measures ground displacement by exploiting the measured phase difference (usually referred to as interferogram) between two SAR images acquired at epochs t_b and t_a [*Gabriel et al.*, 1989; *Massonnet and Feigl*,

1998; *Rosen et al.*, 2000]. The raw interferogram, $\Delta\phi_{raw}(t_a, t_b)$, can be represented as follows,

$$\Delta\phi_{raw}(t_b, t_a) = \Delta\phi_{def}(t_b, t_a) + \Delta\phi_{atmo}(t_b, t_a) + \Delta\phi_{orb}(t_b, t_a) + \Delta\phi_{noise}(t_b, t_a). \quad (1)$$

The raw interferogram is a function of the phase contributions due to the ground deformation between t_b and t_a, $\Delta\phi_{def}(t_b, t_a)$; due to the difference in atmospheric delay between t_b and t_a, $\Delta\phi_{atmo}(t_b, t_a) = \Delta\phi_{atmo}(t_b) - \phi_{atmo}(t_a)$; due to the orbital separation between the satellite at t_b and t_b (spatial baseline), $\Delta\phi_{orb}(t_b, t_a)$ (describing the Earth curvature and topography); and due to the phase noise, $\Delta\phi_{noise}(t_b, t_a)$. We consider all phase contributions to be relative quantities related to differences between the two acquisitions with the exception of $\Delta\phi_{atmo}(t_b, t_a)$. $\Delta\phi_{atmo}(t_b, t_a)$ can be decomposed into atmospheric contribution of each SAR acquisition $\Delta\phi_{atmo}(t_b, t_a) = \phi_{atmo}(t_b) - \phi_{atmo}(t_a)$, with $\phi_{atmo}(t_a)$ and $\phi_{atmo}(t_b)$ as the atmospheric delays at t_a and t_b. $\Delta\phi_{noise}(t_b, t_a)$ has components relating to particular acquisitions (thermal noise) and to the image pair (e.g., changes in the ground dielectric properties, spatial decorrelation, and processing artifacts related to interpolation and interferogram formation) [*Lanari et al.*, 2007].

[11] The orbital phase is modeled using information about the satellite orbits, which are only imperfectly known. The true orbital phase $\Delta\phi_{orb}(t_b, t_a)$ is given by

$$\Delta\phi_{orb}(t_b, t_a) = \Delta\phi^0_{orb}(t_b, t_a) + \Delta\phi^{\varepsilon}_{orb}(t_b, t_a), \quad (2)$$

with $\Delta\phi^0_{orb}(t_b, t_a)$ as the initial orbital phase based on the available satellite orbits and $\Delta\phi^{\varepsilon}_{orb}(t_b, t_a)$ as the orbital phase error (OPE) related to the orbit errors and described in detail below. The differential interferogram, $\Delta\phi(t_b, t_a)$ is obtained by subtracting the initial orbital phase from the raw interferogram,

$$\Delta\phi(t_b, t_a) = \Delta\phi_{raw}(t_b, t_a) - \Delta\phi^0_{orb}(t_b, t_a). \quad (3)$$

Substitution of (1) into (3) using (2) yields the following expression for the differential interferogram,

$$\Delta\phi(t_b, t_a) = \Delta\phi_{def}(t_b, t_a) + \Delta\phi_{atmo}(t_b, t_a) + \Delta\phi^{\varepsilon}_{orb}(t_b, t_a) + \Delta\phi_{noise}(t_b, t_a). \quad (4)$$

3.2. InSAR Time Series

[12] To obtain the temporal evolution of ground deformation, we use many SAR acquisitions of the same area and the small baseline subset (SBAS) method [*Berardino et al.*, 2002; *Lanari et al.*, 2007]. In this approach, the key idea is to select interferometric pairs with small spatial and temporal separation in order to minimize spatial and temporal decorrelation, thus maximizing the number of temporally coherent pixels [*Pepe and Lanari*, 2006]. The baseline thresholds (the maximum spatial baseline and the maximum time span between acquisitions) depend on the type of environment. Sparsely vegetated environments with little topography allow for larger thresholds than heavily vegetated environments with significant topography.

[13] In the SBAS algorithm, a set of Q phase-unwrapped interferograms, $\Delta\phi$p, with $p = 1, \ldots, Q$, is generated from a sequence of N acquisitions at epochs $(t_1, \ldots, t_N)$. These interferograms are subsequently inverted for the phase at epoch t_i with respect to the first acquisition $\phi(t_1)$,

$$\phi(t_i) = \phi_{def}(t_i) + \phi_{atmo}(t_i) + \phi^{\varepsilon}_{orb}(t_i) + \phi_{noise}(t_i), \quad \text{with } i = 2, \ldots, N, \quad (5)$$

with $\phi_{def}(t_i)$, $\phi_{atmo}(t_i)$, $\phi^{\varepsilon}_{orb}(t_i)$, and $\phi_{noise}(t_i)$ as the phase due to deformation, atmosphere, orbital error, and noise with respect to the first acquisition, respectively. The phase contributions at the first epoch cannot be estimated because of the rank deficiency of the system. $\phi_{noise}(t_i)$ now also contains phase-unwrapping errors. Note that interferograms including the first acquisition directly measure $\phi(t_i)$,

$$\phi(t_i) = \Delta\phi(t_i, t_1), \quad (6)$$

and similarly for $\phi_{def}(t_i)$, $\phi_{atmo}(t_i)$, $\phi^{\varepsilon}_{orb}(t_i)$, and $\phi_{noise}(t_i)$. Throughout the reminder of this paper, we only consider phase contributions with respect to the first acquisition.

[14] The objective of crustal deformation studies is to recover $\phi_{def}(t_i)$ from $\phi(t_i)$, thus requiring the estimation of $\phi_{noise}(t_i)$, $\phi_{atmo}(t_i)$, and $\phi^{\varepsilon}_{orb}(t_i)$, which is described in the next three sections.

3.3. Temporal Coherence

[15] The phase noise $\phi_{noise}(t_i)$ is quantified using the temporal coherence. The SBAS analysis is typically carried out using spatially averaged (multilooked) interferograms [*Rosen et al.*, 2000]. We select the coherent pixels for each multilooked interferograms by computing the spatial coherence; the coherent pixels are then used to phase-unwrap each interferogram before inversion for $\phi(t_i)$. For each pixel, we then compute a temporal coherence factor defined as,

$$\gamma = \frac{\left| \sum_{p=1}^{Q} \exp\left[j\left(\Delta\phi_p - \overline{\Delta\phi_p}\right)\right] \right|}{Q}, \qquad 0 \le \gamma \le 1, \quad (7)$$

where $\Delta\phi_p$ is the phase of the original pth interferogram and $\overline{\Delta\phi_p}$ is the phase of the corresponding synthetic interferogram generated by differencing the phase of the computed time series for the two epochs of the pth interferogram. Low temporal coherence arises from inconsistencies of the phase between original and synthetic interferograms. The main causes are decorrelation effects and errors during phase unwrapping of the interferograms. For pixels with $\gamma \to 1$, we expect no errors since a nearly perfect retrieval of the original phase has been obtained. In the following we consider only pixel with γ above a certain threshold. For these pixels, we assume $\phi_{noise}(t_i) = 0$ for $i = 1, \ldots, N$ and equation (5) simplifies to

$$\phi(t_i) = \phi_{def}(t_i) + \phi_{atmo}(t_i) + \phi^{\varepsilon}_{orb}(t_i), \text{ with } i = 2, \ldots, N. \quad (8)$$

3.4. Atmospheric Filtering

[16] The atmospheric phase $\phi_{\text{atmo}}(t_i)$ is the difference between the atmospheric phase screen at epoch t_i and at the epoch of the first acquisition t_1. The atmospheric phase screen is estimated using a spatial-temporal filter [*Ferretti et al.*, 2001; *Berardino et al.*, 2002], assuming that atmospheric phase contributions are spatially correlated and temporally uncorrelated. We apply a low-pass spatial filter followed by a high-pass temporal filter to $\phi(t_i)$. We assume that the estimated atmospheric phase screen $\widehat{\phi}_{\text{atmo}}(t_i)$ equals the atmospheric phase screen $\phi_{\text{atmo}}(t_i)$, i.e., that the atmospheric phase screen error $\phi^{\varepsilon}_{\text{atmo}}(t_i)$ is negligible. We retrieve the atmospheric phase screen at the epoch of the first acquisition assuming that the atmospheric phase screen has zero mean,

$$\phi_{\text{atmo}}(t_1) \approx \frac{1}{N-1}\sum_{i-2}^{N} \widehat{\phi}_{\text{atmo}}(t_i). \tag{9}$$

Subtraction of $\phi_{\text{atmo}}(t_i)$ from $\phi(t_i)$ leads to the filtered phase with respect to the first acquisition $\phi_{\text{filt}}(t_i)$,

$$\phi_{\text{filt}}(t_i) = \phi(t_i) - \phi_{\text{atmo}}(t_i). \tag{10}$$

Substituting (10) into (8) gives

$$\phi_{\text{filt}}(t_i) = \phi_{\text{def}}(t_i) + \phi^{\varepsilon}_{\text{orb}}(t_i), \text{ with } i = 2, \ldots, .N. \tag{11}$$

3.5. Orbital Phase Error

[17] The initial orbits used for InSAR processing of ERS-1 and ERS-2 satellites deviate from the true orbits by about 15 cm on average [*Scharroo*, 2002]. The initial orbit, at epoch t_i, $o^0(t_i)$, relates to the true orbit, $o(t_i)$, as

$$o(t_i) = o^0(t_i) + o^{\varepsilon}(t_i), \tag{12}$$

with $o^{\varepsilon}(t_i)$ as the orbital error we are seeking to estimate. In practice, the spatial separation between the satellites during image acquisition (baseline) is used. For an interferogram between SAR images at epochs t_b and t_a, the baseline $b(t_b, t_a)$ is given by $b(t_b, t_a) = \Delta o(t_b, t_a) = o(t_b) - o(t_a)$. The baseline at epoch t_i, $b(t_i)$, is the difference between the orbit at epoch t_i and the orbit of the first acquisition $o(t_1)$,

$$b(t_i) = o(t_i) - o(t_1), \tag{13}$$

with $i = 2, \ldots, N$. The initial baseline at epoch t_i, $b^0(t_i)$, relates to the true baseline, $b(t_i)$, as

$$b(t_i) = b^0(t_i) + b^{\varepsilon}(t_i), \tag{14}$$

with $b^{\varepsilon}(t_i)$ as the baseline error. The baseline error relates to the orbital error as

$$b^{\varepsilon}(t_i) = o^{\varepsilon}(t_i) + o^{\varepsilon}(t_1). \tag{15}$$

[18] The orbital phase $\phi_{\text{orb}}(t_i)$ at epoch t_i (due to the Earth curvature and topography) is linearly related to the baseline [*Hanssen*, 2001, equation (2.4.18)],

$$\phi_{\text{orb}}(t_i) = b_{\text{h}}(t_i)F_{\text{h}} - b_{\text{v}}(t_i)F_{\text{v}}, \tag{16}$$

with b_{h} and b_{v} as the horizontal and vertical baseline components, respectively, and $F_{\text{h,v}}$ as two factors as

$$F_{\text{h}} = \left(4\frac{\pi}{\lambda}\right)\left(\sin\vartheta - \frac{\cos\vartheta}{\sin\vartheta}\frac{H}{R}\right) \text{and} \tag{17}$$

$$F_{\text{v}} = \left(4\frac{\pi}{\lambda}\right)\left(-\cos\vartheta - \frac{H}{R}\right). \tag{18}$$

H is the terrain height above the ellipsoid, R is the distance between the ground and the satellite (range), and ϑ is the angle at which the radar looks at the surface (look angle).

[19] The initial orbital phase based on the initial orbits $\phi^0_{\text{orb}}(t_i)$ relates to the true orbital phase $\phi_{\text{orb}}(t_i)$ as

$$\phi_{\text{orb}}(t_i) = \phi^0_{\text{orb}}(t_i) + \phi^{\varepsilon}_{\text{orb}}(t_i), \tag{19}$$

with $\phi^{\varepsilon}_{\text{orb}}(t_i)$ as the orbital phase error. We thus can express the orbital phase error in terms of the horizontal and vertical baseline errors, $b^{\varepsilon}_{\text{h}}(t_i)$ and $b^{\varepsilon}_{\text{v}}(t_i)$, as

$$\phi^{\varepsilon}_{\text{orb}}(t_i) = b^{\varepsilon}_{\text{h}}(t_i)F_{\text{h}} - b^{\varepsilon}_{\text{v}}(t_i)F_{\text{v}}. \tag{20}$$

The task is to estimate $b^{\varepsilon}_{\text{h}}(t_i)$ and $b^{\varepsilon}_{\text{v}}(t_i)$, from which $\phi^{\varepsilon}_{\text{orb}}(t_i)$ can be estimated.

3.5.1. OPE Estimation in the Presence of Deformation

[20] We estimate $b^{\varepsilon}_{\text{h}}(t_i)$ and $b^{\varepsilon}_{\text{v}}(t_i)$ at each epoch t_i by minimizing:

$$\min\left\{\phi_{\text{filt}}(t_i) - \phi_{\text{def}}(t_i) - \phi^{\varepsilon}_{\text{orb}}(t_i)\right\}. \tag{21}$$

In the absence of deformation, i.e., for $\phi_{\text{def}}(t_i) = 0$, we estimate $b^{\varepsilon}_{\text{h}}(t_i)$ and $b^{\varepsilon}_{\text{v}}(t_i)$ from $\phi_{\text{filt}}(t_i)$ (i.e., from InSAR only). In the presence of deformation, we estimate $b^{\varepsilon}_{\text{h}}(t_i)$ and $b^{\varepsilon}_{\text{v}}(t_i)$ using a priori information on $\phi_{\text{def}}(t_i)$ as described below. Note that in the classical SBAS approach [*Berardino et al.*, 2002] it is assumed that $\phi^{\varepsilon}_{\text{orb}}(t_i)$ is a simple linear function which is estimated and then removed from $\phi_{\text{filt}}(t_i)$.

[21] Continuous GPS measurements provide displacement at epoch t_i, at radar range location r and radar azimuth location a, $\phi_{\text{def}}(t_i, r, a)$. Because of the pointwise nature of CGPS measurements and the number of available CGPS stations in the InSAR footpath, we approximate the along-track variation of $b^{\varepsilon}_{\text{h}}(t_i)$ and $b^{\varepsilon}_{\text{v}}(t_i)$ by second-order polynomials,

$$b^{\varepsilon}_{\text{h}}(t_i) = c_1(t_i)a^2 + c_2(t_i)a + c_3(t_i), \tag{22}$$

$$b^{\varepsilon}_{\text{v}}(t_i) = c_4(t_i)a^2 + c_5(t_i)a + c_6(t_i), \tag{23}$$

with a as the azimuth coordinate. Equation (20) takes the form

$$\phi^{\varepsilon}_{\text{orb}}(t_i) = \left(c_1(t_i)a^2 + c_2(t_i)a + c_3(t_i)\right)F_{\text{h}} - \left(c_4(t_i)a^2 + c_5(t_i)a + c_6(t_i)\right)F_{\text{v}}. \tag{24}$$

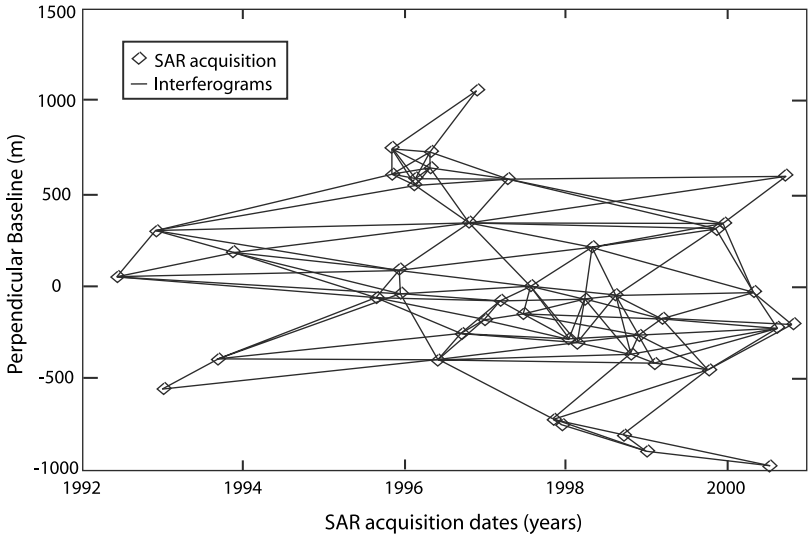

Figure 2. Perpendicular and temporal baselines of SAR acquisitions used in this study. Line segments represent the network of interferograms used for the time series inversion.

[22] At each epoch, $\phi^{\varepsilon}_{\mathrm{orb}}(t_i)$ is thus described by six parameters, $c_1,\ldots,_6$; thus, we estimate $b^{\varepsilon}_{\mathrm{h}}(t_i)$ and $b^{\varepsilon}_{\mathrm{v}}(t_i)$ by minimizing,

$$\min\left\{\sum_{m=1}^{M}\left(\phi_{\mathrm{filt}}(t_i,r_m,a_m)-\phi_{\mathrm{def}}(t_i,r_m,a_m)-\phi^{\varepsilon}_{\mathrm{orb}}(t_i,r_m,a_m)\right)^2\right\}. \tag{25}$$

[23] If deformation is known at six locations ($m = 6$), we solve a system of six equations with the six unknowns $c_1,\ldots,_6$ at each epoch t_i. Note that the estimation of $\phi^{\varepsilon}_{\mathrm{orb}}(t_i)$ and $b^{\varepsilon}_{\mathrm{h,v}}(t_i)$ is associated with errors,

$$\phi^{\varepsilon}_{\mathrm{orb}}(t_i)=\widehat{\phi}^{\varepsilon}_{\mathrm{orb}}(t_i)+\phi^{\varepsilon^{\varepsilon}}_{\mathrm{orb}}(t_i), \tag{26}$$

$$b^{\varepsilon}_{\mathrm{h,v}}(t_i)=\widehat{b}^{\varepsilon}_{\mathrm{h,v}}(t_i)+b^{\varepsilon^{\varepsilon}}_{\mathrm{h,v}}(t_i), \tag{27}$$

with $\widehat{\phi}^{\varepsilon}_{\mathrm{orb}}(t_i)$ and $\widehat{b}^{\varepsilon}_{\mathrm{h,v}}(t_i)$ as the estimated orbital phase error and baseline component errors, respectively, and $\phi^{\varepsilon^{\varepsilon}}_{\mathrm{orb}}(t_i)$ and $b^{\varepsilon^{\varepsilon}}_{\mathrm{h,v}}(t_i)$ as the respective estimation errors.

[24] After subtraction of $\phi^{\varepsilon}_{\mathrm{orb}}(t_i)$ from $\phi_{\mathrm{filt}}(t_i)$, we have achieved our objective of recovering $\phi_{\mathrm{def}}(t_i)$.

4. Integration of InSAR Time Series and CGPS: Application to ECSZ

4.1. Large-Scale SBAS Processing

[25] In the past, the SBAS technique has mostly been applied to investigate deformation of areas typically extending ~100 × 100 km^2. In this study, we use the SBAS technique to study a larger area (~600 × 100 km^2) [*Casu et al.*, 2008].

[26] We analyze a set of 44 ERS-1/2 SAR swaths (track 442, frames 2781–2871), spanning the 1992–2000 time interval. To reduce the amount of data to be processed, the image resolution is degraded to a pixel size of 160 × 160 m^2 compared to 80 × 80 m^2 for conventional SBAS processing.

[27] The interferometric pairs are selected using a maximum spatial and temporal baseline of 400 m and 1500 days, respectively (Figure 2); by applying these constraints, 148 multilook interferograms are generated. The interferograms are phase-unwrapped and subsequently inverted for the phase with respect to the first acquisition $\phi(t_i)$.

4.2. Temporal Coherence

[28] The temporal coherence estimated using equation (7) is shown in Figure 3a. Most of the low-topography areas, including the basins, exhibit high coherence (larger than 0.7). The mountain ranges are characterized by low coherence (near 0), including the Sierra Nevada in the southwest. The loss of coherence occurs because the surface characteristics change with time. In the mountains, coherence is lost because of temporary snow cover. In some valleys, coherence may be lost because of flooding. Another reason for coherence loss in the mountains is geometric decorrelation related to the steep slopes. In this study, we use only pixel with temporal coherence larger than 0.7 shown in Figure 3b.

4.3. Atmospheric Filtering

[29] In order to quantify the efficiency of the atmospheric filtering, we perform a 1-D covariance analysis [*Hanssen*, 2001] on the phase before and after filtering ($\phi(t_i)$ and $\phi_{\mathrm{filt}}(t_i)$, respectively). At each epoch, we conduct an autocorrelation and model the resulting amplitude by a two-parameter Bessel function following *Biggs et al.* [2007] (Figures 4a and 4b). Figure 4 shows that the spatial-temporal filtering reduces the correlation amplitude and length in average by 30%.

[30] The atmospheric filtering is illustrated in map view in Figure 5. Figure 5 shows the phase at the 23 November 1992 epoch before and after filtering (Figures 5a and 5d, respectively) as well as the estimated $\phi_{\mathrm{atmo}}(t_i)$ for the first acquisition (1 June 1992, Figure 5b) and for the 23 November 1992 acquisition (Figure 5c). The phase at epoch 23 November 1992 corresponds to the interferogram

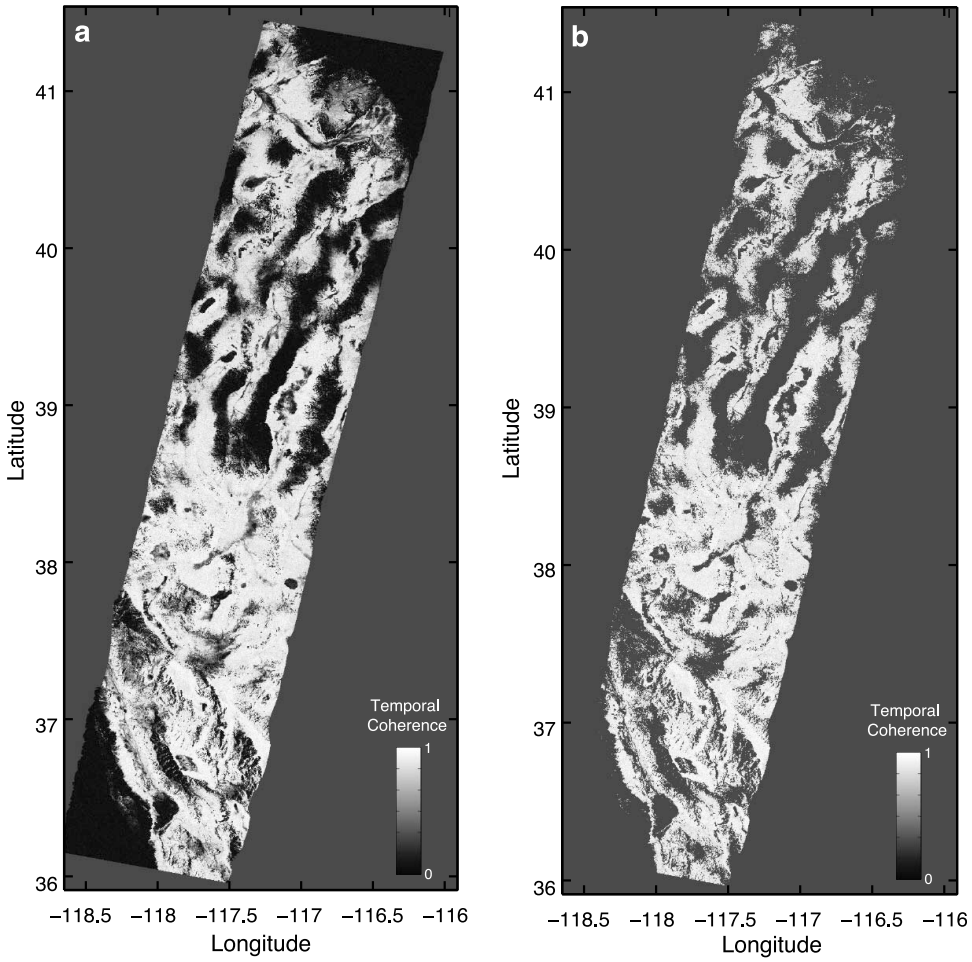

Figure 3. (a) Temporal coherence γ. (b) Coherence mask using a threshold of 0.7.

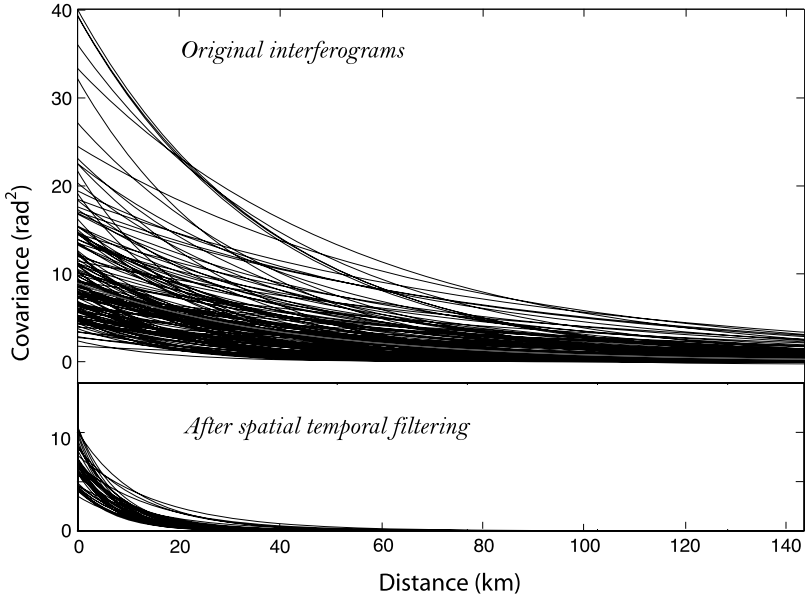

Figure 4. Phase covariance as a function of distance between pixel for each of the 44 epochs (a) before and (b) after spatial-temporal filtering. The filtering reduces both the magnitude and length of the correlated noise by about 40%.

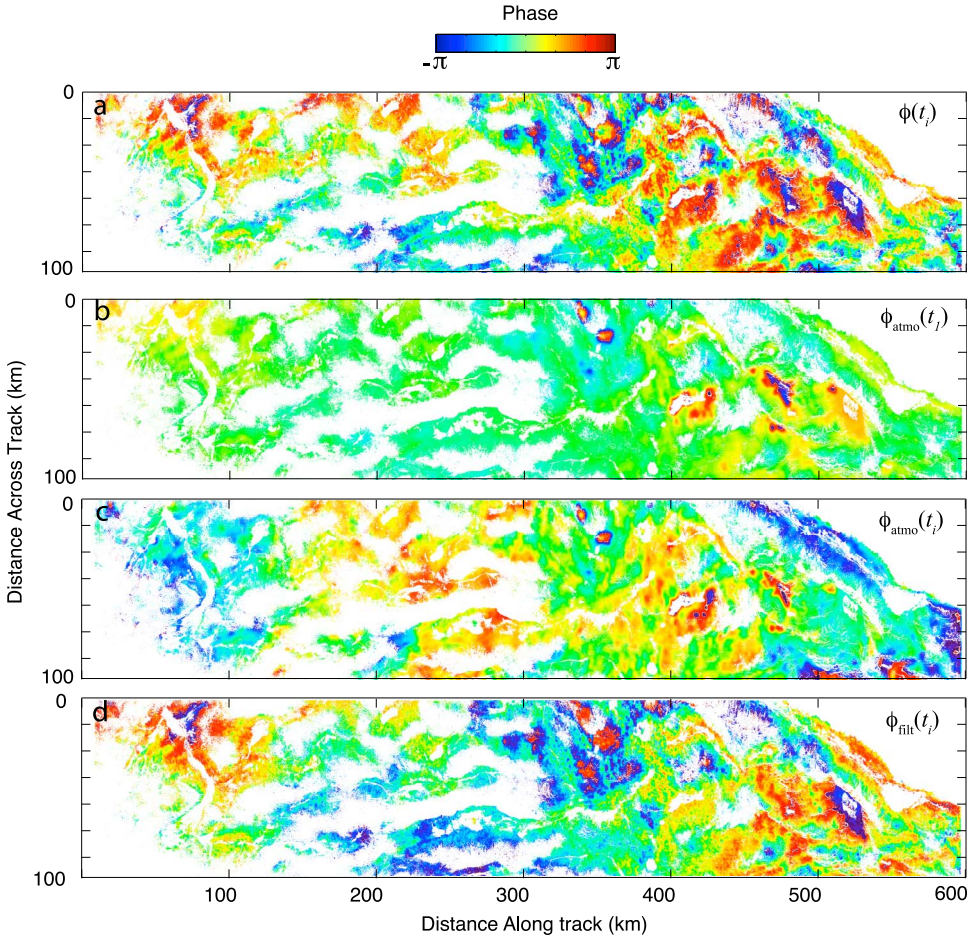

Figure 5. Example of the phase at a given epoch before and after atmospheric filtering: (a) phase before atmospheric filtering at epoch $t_i = 23$ November 1992, $\phi(t_i)$; (b) estimated atmospheric phase screen for reference epoch $t_1 = 1$ June 1992, $\phi_{atmo}(t_1)$; (c) estimated atmospheric phase screen for epoch $t_i = 23$ November 1992, $\phi_{atmo}(t_i)$; and (d) filtered phase at epoch $t_i = 23$ November 1992 obtained using equation (10), $\phi_{filt}(t_i)$.

between the 6 June 1992 and 23 November 1992 acquisitions because the first acquisition of the interferogram is also the reference epoch of the time series (see equation (10)).

[31] The estimated baseline error for the 23 November 1992 epoch with and without atmospheric filtering is shown in Figure 6. The differences are generally only a few centimeters, with several meters locally, indicating that atmospheric filtering has only little effect on the estimated baseline error.

4.4. Baseline Errors and the Effect of Ground Deformation on Their Estimation

[32] The baseline errors for five epochs, estimated using the assumption of no deformation, $\phi_{def}(t_i) = 0$, are shown as function of azimuth in Figure 7. The estimated baseline errors ($\widehat{b}^{\varepsilon}_{h}(t_i)$ and $\widehat{b}^{\varepsilon}_{v}(t_i)$) along most of the SAR swath is less than 15 m (Figures 7a and 7b). This is much larger than the orbital error estimates of *Scharroo* [2002], but similar to values obtained using the baseline reestimation inversion

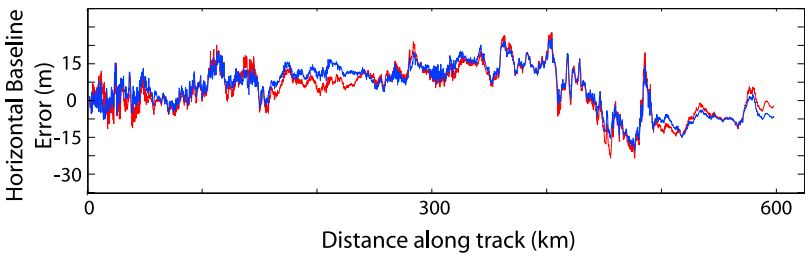

Figure 6. Horizontal baseline error at epoch $t_i = 23$ November 1992, $\widehat{b}^{\varepsilon}_{h}(t_i)$, obtained from equation (21) and substituting equation (20) before (red line) and after atmospheric filtering (blue line), assuming $\phi_{def}(t_i) = 0$.

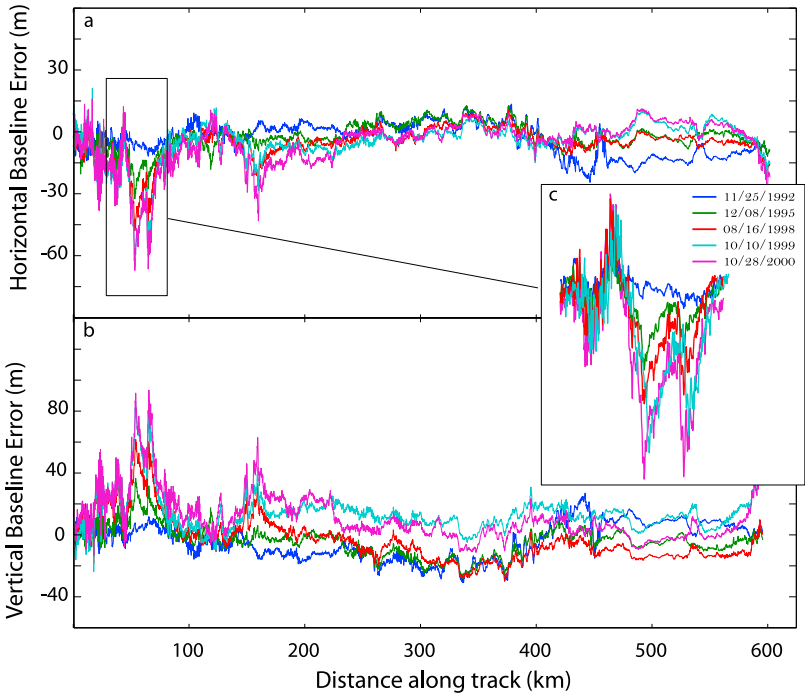

Figure 7. (a) Horizontal and (b) vertical baseline error, $\widehat{b}^{\varepsilon}_{\mathrm{h,v}}(t_i)$, for five example epochs estimated assuming $\phi_{\mathrm{def}}(t_i) = 0$. (c) Zoom into horizontal baseline error for the subsiding Crescent Valley area (see Figure 13) and epochs of SAR acquisitions. The large variations of the estimated baseline error in the subsidence area illustrate that deformation needs to be taken into account for baseline error estimation.

strategy based on topographic information used in JPL's ROI_PAC software [*Rosen et al.*, 2004]. At the beginning of the SAR swath (at 40–100 km along-track distance, Figure 7c) and at the end of the swath (at 400–600 km along-track distance), the estimated baseline error is up to 60 and 30 m, respectively (Figure 7c). This is caused by the assumption that $\phi_{\mathrm{def}}(t_i) = 0$. The effect of surface displacement on the estimated baseline error is clearly illustrated by the retrieved baseline correction term in the subsiding region of the Crescent Valley area (Figure 8), where we see a linear correlation between the estimated baseline error $\widehat{b}^{\varepsilon}_{\mathrm{h}}(t_i)$ and the surface deformation $\phi_{\mathrm{def}}(t_i)$. We conclude from this section that $\phi_{\mathrm{def}}(t_i)$ needs to be taken into account for the estimation of the baseline errors.

4.5. OPE Estimation Using GPS

4.5.1. GPS Data

[33] We use continuous GPS (CGPS) as a measure of $\phi_{\mathrm{def}}(t_i)$. We use six CGPS stations from the PBO core network (previously referred to as BARGEN network) [*Wernicke et al.*,2000; *Bennett et al.*, 2003; *Davis et al.*, 2006] located in the area imaged by the SAR (Figure 9). The stations are distributed evenly over the entire SAR track. Two stations are located on the stable Basin and Range block (MONI and TONO), two stations are located in the vicinity of the Central Nevada Seismic Belt (GABB, NEWS), and two stations are located in the vicinity of the ECSZ (ARGU, COSO, and DYER). There are two additional GPS stations with data starting in the mid-1990s (LEWI and COSO), but we could not use them for reasons discussed below. The CGPS positions are referred to a stable Basin and Range reference frame defined by 26 permanent GPS stations located within the stable Basin and Range block [*Schmalzle*, 2008]. We use the GPS records starting in 1999 when all six stations were operating simultaneously.

[34] In the following, we consider the GPS displacement component in radar line-of-sight (LOS) direction, obtained

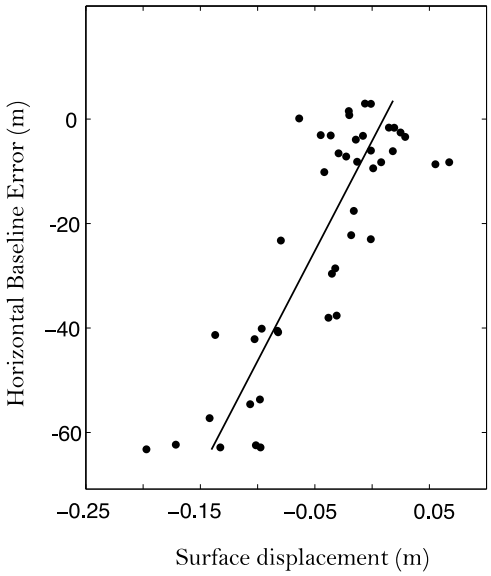

Figure 8. Horizontal baseline errors for all epochs $\widehat{b}^{\varepsilon}_{\mathrm{h}}(t_i)$ estimated assuming $\phi_{\mathrm{def}}(t_i) = 0$ versus surface displacement and linear fit for a pixel in the subsiding Crescent Valley area (at 70 km distance along track on Figure 7).

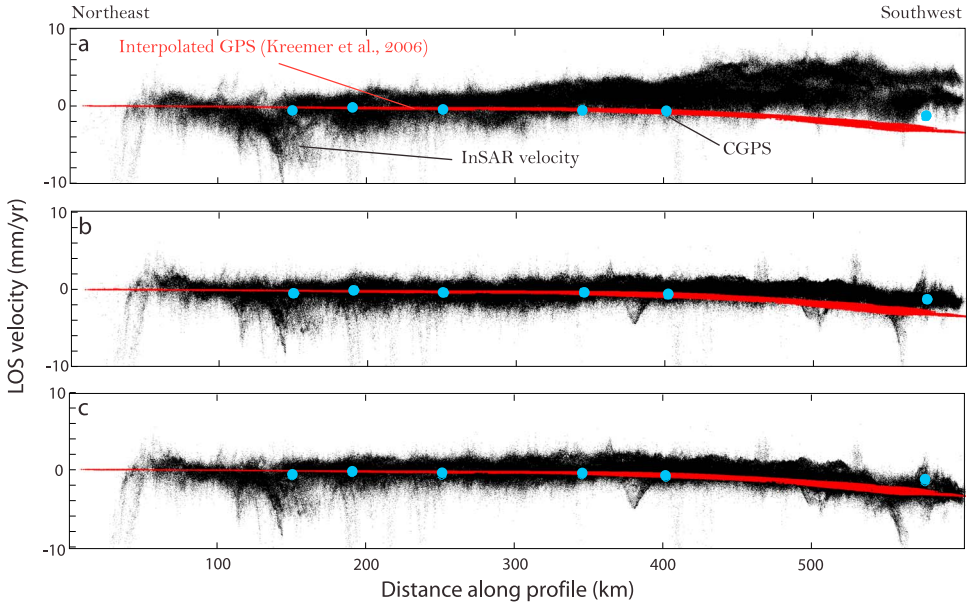

Figure 9. GPS velocity (red and blue) and InSAR velocity (black) in LOS direction projected along a profile perpendicular to the ECSZ (see Figure 13) for location of the profile between 300 and 600 km: (a) InSAR velocity without OPE removal, (b) InSAR velocity with OPE removal not accounting for deformation, and (c) InSAR velocity with OPE removal using the CGPS measurements to account for deformation. LOS velocity of the six CGPS stations used in the inversion (blue dots). At a distance along the profile of 0 km, the InSAR, GPS, and CGPS profiles have been arbitrarily adjusted to 0 mm/yr.

by multiplying the east, north, up GPS vector with the unit vector pointing from the ground to the radar [0.3, −0.09, 0.9] in [east, north, up].

4.5.2. GPS Velocity Field

[35] For the comparison of the InSAR with the GPS, we use the interpolated horizontal velocity field of the Basin and Range region from the work of *Kreemer et al.* [2006]. This velocity field is based on campaign and continuous data with records of a few years to over 15 years with large station density variations (the station density is higher near the active volcanic and seismic region of the Sierra Nevada–Basin and Range boundary). The GPS velocity field includes data of the high-density, semipermanent MAGNET network operated by the University of Nevada, Reno. *Kreemer et al.* obtained this spatially continuous velocity field (on a 0.2° × 0.2° grid) from the GPS point measurements by interpolating the GPS velocities in a least squares sense using a bicubic Bessel spline function. For the analysis below this velocity field is transformed into LOS direction assuming zero vertical deformation.

4.5.3. Comparison Between InSAR and Interpolated GPS Velocity Field

[36] To illustrate the effect of OPE on the calculated InSAR ground velocity and time series, we compare the ground velocity data from InSAR with continuous GPS and the interpolated GPS velocity field. To do so, we project all data sets (LOS component for the GPS) along a profile perpendicular to the ECSZ (in N60°W direction) (Figure 9). The InSAR data are shown without OPE removal (Figure 9a), with OPE removal assuming zero deformation (Figure 9b), and with OPE removal accounting for deformation using the continuous GPS data (Figure 9c).

[37] Without OPE removal, there is a general disagreement between the InSAR and GPS (Figure 9a). At 400–600 km along the profile, the difference is on the order of 4–8 mm/yr. The nature of the velocity difference is similar to the work of *Burgmann et al.* [2006], although we observe a lower gradient, 0.03 mm/yr/km. With OPE removal assuming zero deformation, the InSAR and GPS data are roughly consistent in the northeast (0–400 km along profile), but there is a discrepancy in the southeast of about 2–3 mm/yr (Figure 9b). Note that scatter is less when the OPE is removed (Figure 9b compared with Figure 9c). The case of OPE removal accounting for deformation (Figure 9c) is discussed below.

4.5.4. Comparison Between InSAR and Continuous GPS

[38] The CGPS stations are located within the mountain ranges, where InSAR data are not available because of decorrelation. We therefore average all coherent InSAR pixel within 2 km radius from each CGPS stations. As a result, we have to eliminate the LEWI and COSO GPS stations from our analysis. Both stations are affected by local deformation and therefore the ground within 2 km from the GPS bench mark may deform differently than the GPS bench mark itself. LEWI is affected by local subsidence due to water withdrawal in support of mining activities [*Gourmelen et al.*, 2007]; COSO is affected by subsidence associated with the nearby Coso geothermal plant [*Bennett et al.*,2003]. We note that GPS stations affected by local deformation can be used for the estimation of orbital phase errors as long as they collocate with coherent pixel.

[39] The InSAR time series are shown together with the CGPS time series in Figure 10a for the six GPS stations. The northernmost stations are plotted at the top and the south-

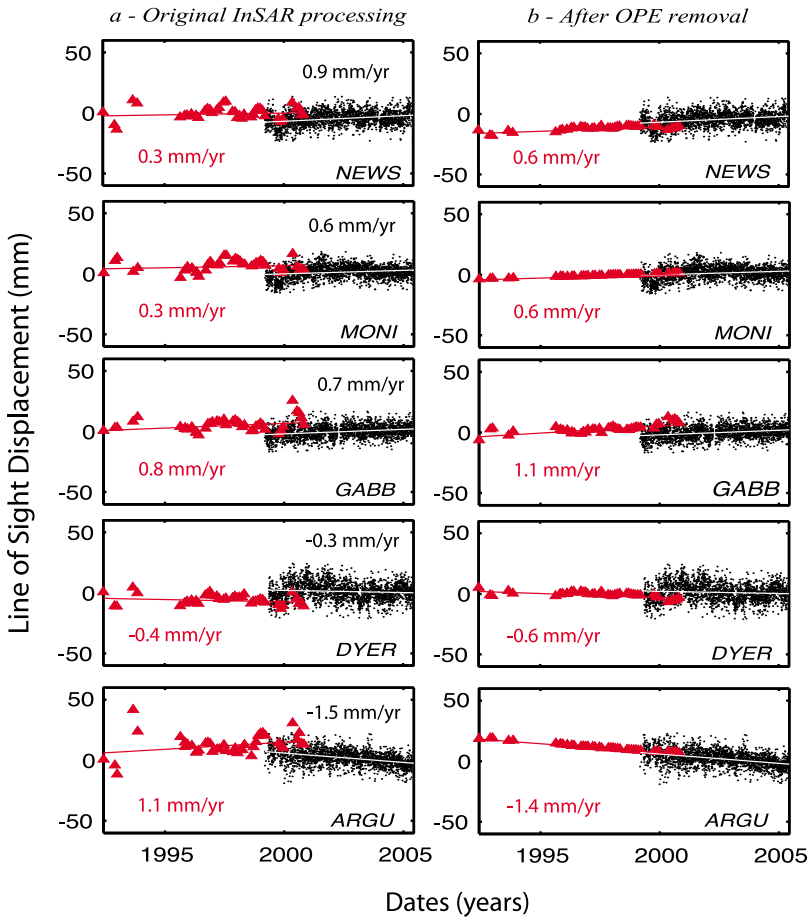

Figure 10. LOS displacement time series from InSAR SBAS analysis and daily positions for six collocated GPS sites in the western Basin and Range. (a) Conventional SBAS analysis after the removal of linear and second-order phase contributions (before calibrations with GPS). (b) SBAS analysis after removal of OPE determined from continuous GPS measurements. We extrapolated the 1999–2005 GPS measurements back to the beginning of SAR measurements in 1992. The InSAR errors are estimated at ±0.6 mm/yr [*Gourmelen et al.*, 2007]; GPS errors of ±0.7 are estimated assuming white and flicker noise [*Dixon et al.*, 2000b].

ernmost stations at the bottom of the frame. The largest differences between InSAR and GPS are found in the southernmost areas, within the ECSZ. For example, ARGU's GPS velocity is −1.5 ± 0.7 mm/yr, whereas the corresponding InSAR velocity is +1.1 ± 0.6 mm/yr, a difference of 2.6 mm/yr. To the north within the stable Basin and Range block MONI's GPS velocity is 0.6 ± 0.7 mm/yr, whereas the corresponding InSAR velocity is 0.3 ± 0.6 mm/yr, a difference of 0.3 mm/yr. This pattern of southwestward increasing differences between InSAR and continuous GPS is similar to differences between the InSAR and the interpolated GPS velocity field from *Kreemer et al.* [2006] (Figure 9).

4.5.5. OPE Correction Using Continuous GPS

[40] The continuous GPS data are complete since 1999 but the InSAR data start in 1992. Therefore, we extrapolate the GPS time series for the 1992–1999 period using the averaged 1999–2005 velocities. This approach yields predicted GPS positions at each SAR epoch.

[41] We then assume a second order azimuth model and apply equation (25) to estimate the OPE and remove it from the InSAR time series at each epoch. The corrected InSAR time series show a significant reduction of the noise level (Figure 10, right). More importantly, the difference between the InSAR and continuous GPS velocities is within the range of error.

[42] The quality of the OPE estimation using GPS is also clearly seen by comparing the InSAR with the interpolated GPS velocity field of *Kreemer et al.* [2006] After OPE removal accounting for deformation (Figure 9c), there is a broad agreement between the InSAR velocities and the interpolated GPS velocities.

4.5.6. Azimuth Model

[43] To evaluate the spatial model used to approximate the OPE, we compute the standard deviation of the phase history for each pixel. Figure 11 shows the standard deviation for the original time series (Figure 11a), after removal of the OPE assuming a linear azimuth model (obtained by substituting equations (22) and (23) by a linear model (Figure 11b) and after removal of the OPE using the quadratic models of equations (22) and (23) (Figure 11c). We also display the phase of the 23 November 1992 epoch as a function of the

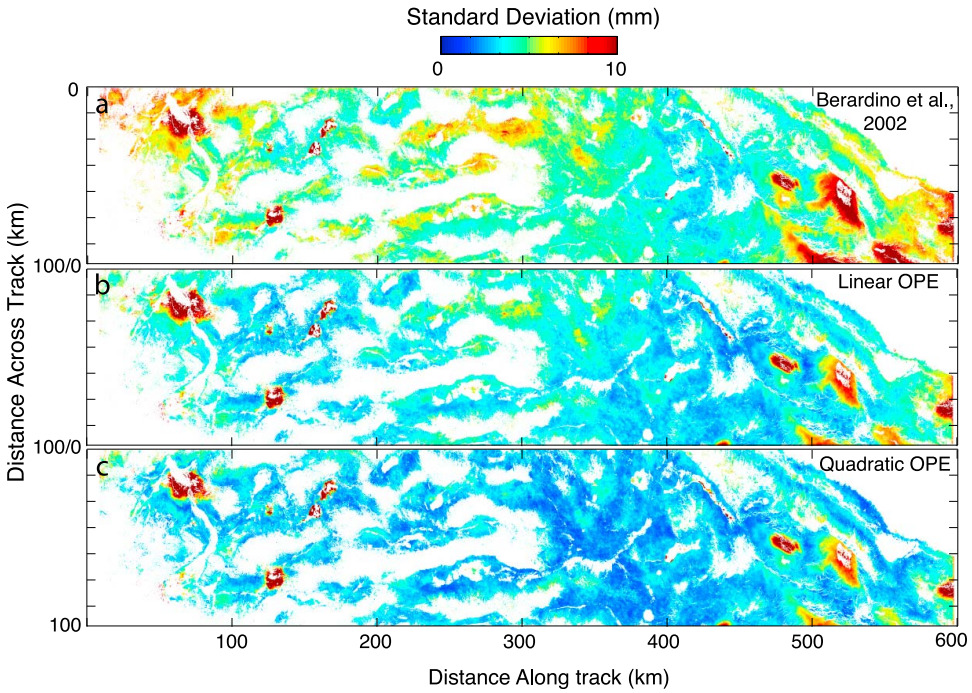

Figure 11. Standard deviation of the time series in function of the orbital model. Quadratic variation of the baseline errors gives the most satisfying results. High residual standard deviation is localized and corresponds to regions of deformation (e.g., subsidence, earthquakes).

model used to remove the OPE (Figure 12). The quadratic model results in the smallest standard deviation and performs well in removing long-wavelength phase residuals, suggesting that a quadratic model is most appropriate. However, the standard deviation criteria has to be taken with caution as strong regional periodical signal typically recorded by GPS, from atmospheric or hydrologic forcing, will tend to increase the standard deviation. These effects are minimized as we consider the GPS record in a local reference frame where atmospheric or hydrologic forcing are homogeneous. Local deformation due to subsidence or earthquakes is associated with a high standard deviation in the threes cases as expected.

4.5.7. InSAR Velocity Map

[44] The average velocity for each coherent pixel, obtained from the filtered time series, is shown in Figure 13. Tightening the color scale between [−4, 4] mm/yr reveals the pattern of deformation across the ECSZ (Figure 14). Little deformation is seen across the Fish Lake Valley–Furnace Creek fault system. Assuming pure strike-slip motion across the fault, taking into account the orientation of the fault with respect to the radar look angle, and the InSAR rate uncertainty of 0.6 mm/yr, we can determine an upper limit of 2 mm/yr of strain accumulation across the fault system. This upper limit can be higher however depending on the deformation's wavelength. The velocity map reveals a sharp and localized deformation along the White Mountain fault; the deformation is localized along a narrow band in the central part of the valley and corresponds to ground subsidence. We attribute this deformation signal to water-related subsidence. With the exception of the subsidence signal, little deformation is measured across the White Mountain–Owens Valley fault system for the same reasons stated for the Fish Lake–Furnace Creek fault system. The upper limit here is 5 mm/yr because of the northerly orientation of the fault system. Instead, most of the signal is located across the Hunter Mountain (HM) fault.

5. Modeling the Strain Accumulation Across the Hunter Mountain Fault

[45] In order to analyze the signal across the Hunter Mountain fault, we remove the Eureka Valley coseismic displacement field [*Peltzer and Rosen*, 1995]. For this, we first divide the displacement time series into a preearthquake and a postearthquake time series. After subtracting linear trends from both time series, we compute the respective mean values and obtain a preearthquake mean position and a postearthquake mean position. We then subtract the preearthquake mean position from the postearthquake mean position to obtain the coseismic offset and subtract it from the displacement at each postearthquake epoch. We then recalculate the velocity map.

[46] A profile perpendicular to the Hunter Mountain fault (Figure 15) reveals a LOS velocity change of 1.6 ± 0.6 mm/yr across the fault. The LOS velocity change occurs progressively across a zone with a width of 5–12 km centered on the fault. Unwrapping errors or atmospheric phase residuals are unlikely to be the cause of the observed signal as temporal coherence masking and atmospheric phase filtering has been applied; this leads us to consider that the signal across the Hunter Mountain fault contains only surface deformation. We observe that a hydrological signal affects the basin north of the Hunter Mountain fault in some of our interferograms. The spatial and temporal characteristics of this signal are similar to the characteristics of atmospheric perturbations

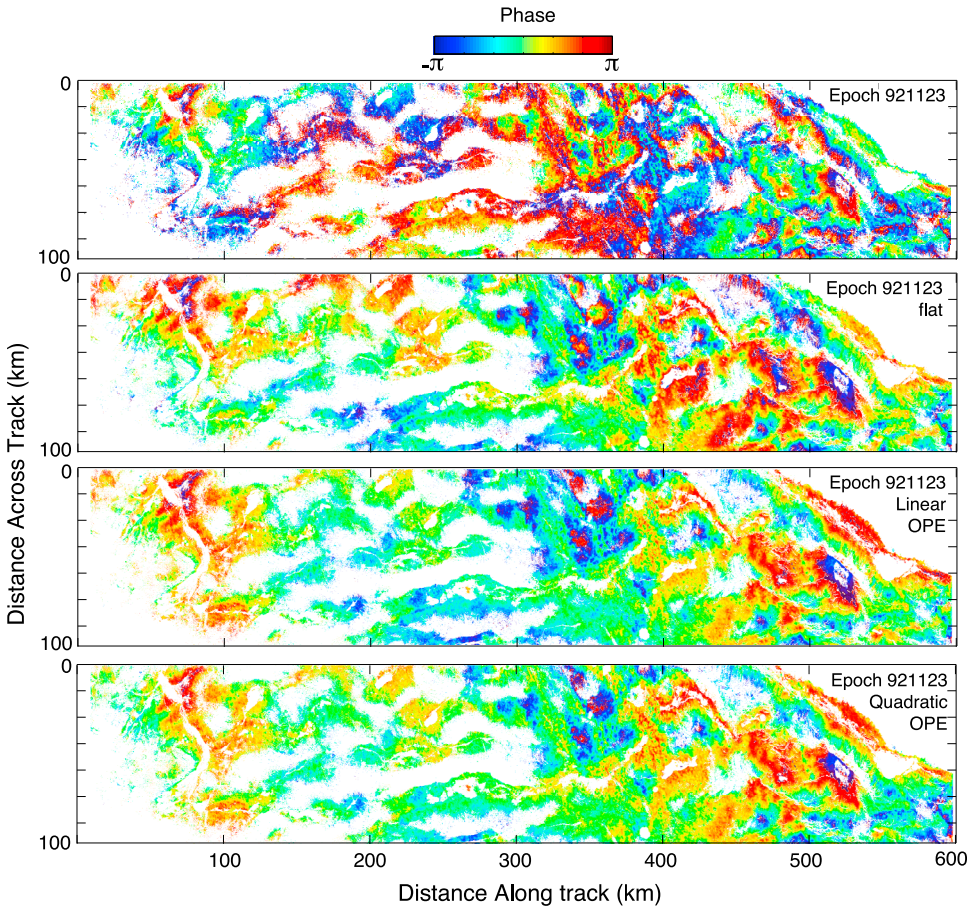

Figure 12. From top to bottom: Phase at 23 November 1992 epoch, phase after flattening, phase after removal of linear orbital model, phase after removal of quadratic orbital model.

and are removed by processing of data over a long time period and by applying spatial and temporal filtering.

[47] We now assume that the velocity change across the Hunter Mountain fault is the result of interseismic strain accumulation along a pure right-lateral strike-slip fault. We note that the lack of a discontinuity suggests that there is no or little surface creep. We use the classical elastic dislocation model of *Savage and Burford* [1973], in which the fault is driven from a freely slipping fault at depth embedded in an elastic half-space. The model has two parameters: the far-field velocity (corresponding to the slip rate of the freely slipping fault at depth) and the locking depth [*Savage and Burford*, 1973; *Weertman and Weertman*, 1964] (Figure 15). We use a nonlinear Gibbs sampling inversion scheme to retrieve the two parameters and their probability density distributions [*Johnson and Segall*, 2004]. This simple model fits the data very well. The best fit is obtained for a slip rate of 4.9 ± 0.8 mm/yr and a locking depth of 2 ± 0.4 km (Figure 16). Note that there is little correlation between the fault slip rate and the locking depth.

[48] Additional modeling of the deformation across the Hunter Mountain fault suggests that neither surface creep nor viscoelastic relaxation is occurring. A model including shallow creep [*Savage and Lisowski*, 1993] predicts no displacement on the shallow creeping section. We also tested models including viscoelastic relaxation, with model parameters locking depth, fault slip rate, time since the last earthquake, recurrence interval, and viscosity [*Savage and Lisowski*, 1998]. The best fitting models are characterized by similar values for the time since the last earthquake and the recurrence time, implying that the viscoelastic relaxation is completed (assuming a viscosity of $10e^{19}$ Pa s) [*Dixon et al.*, 2003; *Thatcher and Pollitz*, 2008]. In conclusion, the InSAR data are well modeled with a simple screw dislocation in an elastic medium and do not require surface fault creep or viscoelastic rheology.

6. Discussion

[49] The InSAR results across the eastern California shear zone reveal a narrow zone of deformation across the Hunter Mountain fault. The observations are well explained using the *Savage and Burford* [1973] elastic dislocation model with a vertical strike-slip fault with a 2 km locking depth and a slip rate of 4.9 mm/yr.

[50] The OPE removal method is not essential to study the deformation across the Hunter Mountain fault as the wavelength of the two processes are very different. However, our method resolves the plane ambiguity resulting from either OPE residuals or large-scale deformation due to nearby faults. The OPE removal shows that the ground deformation across the Hunter Mountain fault results only

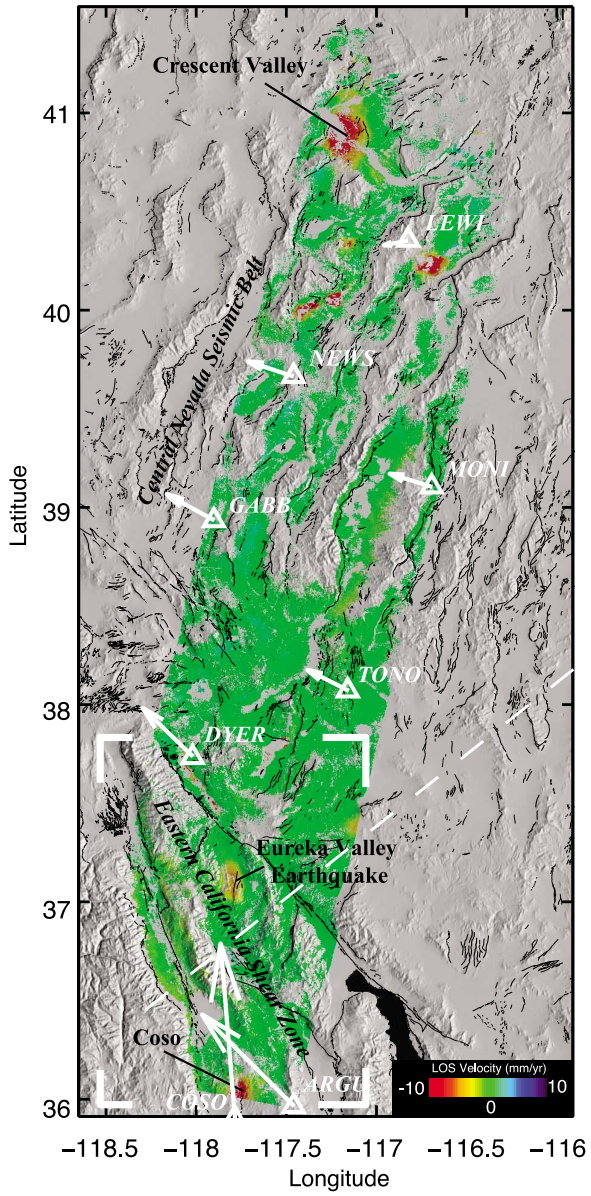

Figure 13. InSAR velocity map across the Basin and Range and horizontal velocity of PBO continuous GPS [*Bennett et al.*, 2003]. Location of Figure 14 in inset. Location of profile perpendicular to ECSZ from Figure 9 between 300 and 600 km distance along profile.

from the Hunter Mountain fault with little effects from the Owens Valley and Death Valley fault systems.

[51] The slip rate of the Hunter Mountain fault estimated from the geodetic data is within the higher end of the range of geologic rates bracketed between 2.4 and 4 mm/yr [*Gourmelen*, 2009]. The geologic rates have been inferred from the total fault offset since fault initiation. One explanation for this difference in rate is that the fault has been accelerating through geologic times. *Gourmelen* [2009] proposed a model of fault evolution in which the slip rate increased as the fault matured and propose a model that accounts for the distribution of slip rate for different periods of activity of the Hunter Mountain fault.

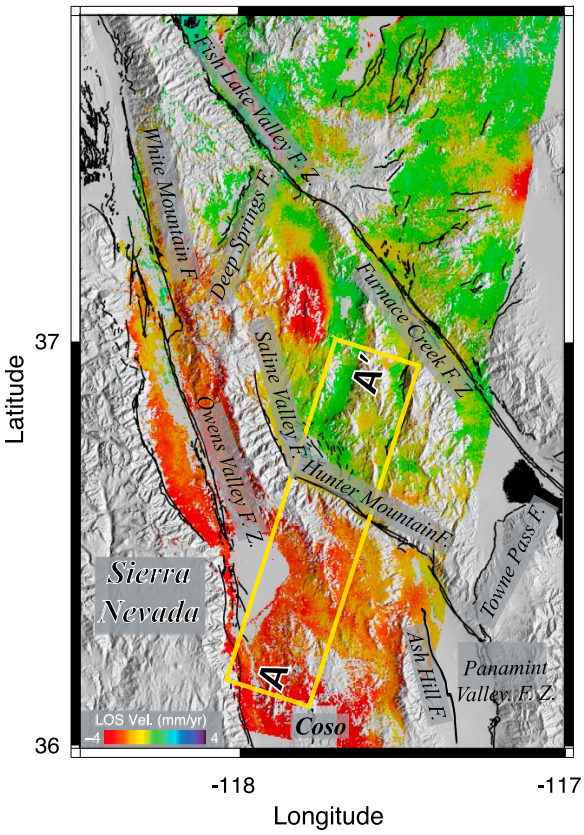

Figure 14. Velocity change across the eastern California shear zone. Yellow box: location of profile in Figure 15.

[52] Our locking depth estimation for the Hunter Mountain fault is significantly shallower than locking depth estimates of nearby faults which generally range between 5 and 15 km [*Dixon et al.*, 2003; *Bennett et al.*, 1997; *Peltzer et al.*, 2001; *McClusky et al.*, 2001; *Gourmelen and Amelung*, 2005;

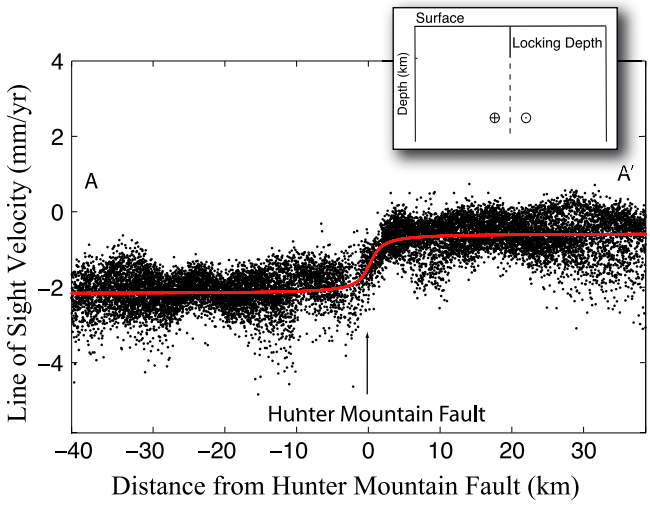

Figure 15. LOS velocity perpendicular to the Hunter Mountain fault. The area covered is shown in Figure 11. Fault and earth models after *Savage and Burford* [1973] in inset.

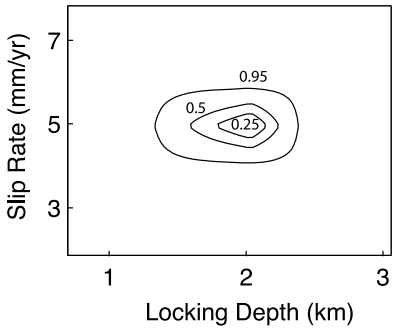

Figure 16. Locking depth versus slip rate probability from Gibbs sampling.

Meade and Hager, 2005]. The area is characterized by shallow seismic activity and shallow magmatism, recording between 1991 and 1995. *Feng and Lees* [1998] determine that microseismicity was localized at a depth of 3 km at the geothermal field likely related to the geothermal exploitation and at a depth of 6 km in the neighboring region. Similarly, local studies by *Walter and Weaver* [1980] and a regional study by [*Sibson*, 1982] find a cutoff depth of the seismicity of 5 km, shallower than for most of California. *Wicks et al.* [2001] argue for a shallow magma body 4 km below the surface below the Coso geothermal plant. This suggests that brittle deformation occurs at shallow depth and that this depth is increasingly shallow toward the Hunter Mountain fault as shown by the shallow locking depth found in this study. These observations would support the low-angle normal fault geometry proposed by *Biehler* [1987] and *Wesnousky and Jones* [1994] (Figure 17). In this system, the Hunter Mountain fault would play the role of a transfer fault which deformation would be driven by the motion of the Panamint and Saline Valley faults. This interpretation is however speculative at this point and would benefit from a more complex modeling of the fault system and surface deformation. If the low-angle fault system was to be active, it would have consequences on the current slip rate estimates over the ECSZ.

7. Conclusion

[53] 1. We review the theoretical framework for orbital phase errors (OPE) in InSAR time series. Orbital phase errors are related to uncertainties in the satellite position during image acquisitions. They impact the ability of InSAR to precisely measure subtle, long-wavelength deformation (over several hundred kilometers).

[54] 2. The orbital phase error at a given epoch can be expressed in terms of the horizontal and vertical baseline errors (difference in satellite position at a given epoch with respect to the first epoch) (equation (20)). The baseline errors at a given epoch are a function of along-track position. Assuming that their along-track variation can be approximated by second-order polynominals, the orbital phase error is described by six parameters (equation (24)). In the absence of deformation, the orbital phase errors can be estimated directly from the InSAR data. In the presence of deformation, they can be estimated using independent information such as from models or GPS (equation (25)).

[55] 3. We apply this method to the eastern California shear zone using 44 ERS SAR acquisitions from 1992 to 2001 and data from six continuous GPS stations starting in 1999. Using this method, InSAR recovers the long-wavelength deformation of the region known from GPS (Figure 9).

[56] 4. The corrected InSAR time series data reveal a region of rapid velocity change across the Hunter Mountain fault. Observed ground deformation is interpreted as caused by interseismic strain accumulation across a strike-slip fault. Modeling with the classical *Savage and Burford* [1973] elastic model suggests a locking depth of 2 ± 0.4 km and a slip rate of 4.9 ± 0.8 mm/yr. There is no evidence for surface creep.

[57] 5. The geodetic slip rate of the Hunter Mountain fault is faster than geologic slip rates, suggesting that the fault has accelerated over time. The locking depth is very shallow in comparison with nearby faults. This may indicate the fault

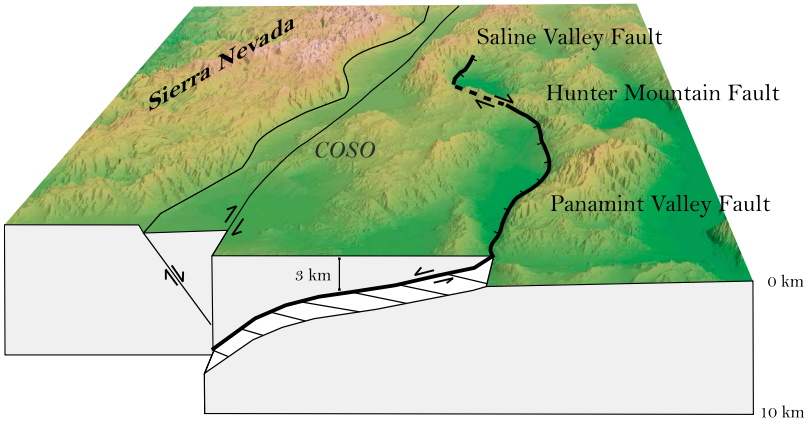

Figure 17. Model of present-day tectonic for the Owens Valley–Panamint Valley–Hunter Mountain–Saline Valley faults modified from *Wesnousky and Jones* [1994]. At the location of the InSAR profile, the depth of the Panamint fault is of the order of the locking depth for the Hunter Mountain fault.

plays a pivotal mechanical role in low angle normal fault system in the area.

[58] **Acknowledgments.** We thank Timothy Dixon and Freek Van Leijen for discussion and two anonymous reviewers for comments that significantly improved the manuscript. We thank Mariarosaria Manzo for her support to the SBAS-DInSAR results handling. We thank the European Space Agency for the SAR data, which were obtained through the GeoEarthscope and WinSAR projects at UNAVCO. NASA supported this research through an Earth System Science fellowship to N.G. and the National Science Foundation through grant NSF-EAR 0454552 to F.A.

References

Amelung, F., S. Jonsson, H. Zebker, and P. Segall (2000), Widespread uplift and "trapdoor" faulting on Galapagos volcanoes observed with radar interferometry, *Nature*, *407*, 993–996.

Bennett, R. A., B. P. Wernicke, J. L. Davis, P. Elosegui, J. K. Snow, M. J. Abolins, M. A. House, G. L. Stirewalt, and D. A. Ferrill (1997), Global positioning system constraints on fault slip rates in the Death Valley region, California and Nevada, *Geophys. Res. Lett.*, *24*, 3073–3076, doi:10.1029/97GL02951.

Bennett, R. A., B. P. Wernicke, N. A. Niemi, A. M. Friedrich, and J. L. Davis (2003), Contemporary strain rates in the northern Basin and Range province from GPS data, *Tectonics*, *22*(2), 1008, doi:10.1029/2001TC001355.

Berardino, P., G. Fornaro, R. Lanari, and E. Sansosti (2002), A new algorithm for surface deformation monitoring based on small baseline differential SAR interferograms, *IEEE Trans. Geosci. Remote Sens.*, *40*(11), 2375–2383.

Biehler, S. (1987), A geophysical investigation of the Northern Panamint Valley, Inyo County, California: Evidence for possible low-angle normal faulting at shallow depth in the crust, *J. Geophys. Res.*, *92*, 10427–10441, doi:10.1029/JB092iB10p10427.

Biggs, J., T. Wright, Z. Lu, and B. Parsons (2007), Multi-interferogram method for measuring interseismic deformation: Denali fault, Alaska, *Geophys. J. Int.*, *170*, 1165–1179.

Burchfiel, B. C., K. V. Hodges, and L. H. Royden (1987), Geology of Panamint Valley–Saline Valley pull-apart system, California – Palinspastic evidence for low-angle geometry of a Neogene range-bounding fault, *J. Geophys. Res.*, *92*, 10422–10426, doi:10.1029/JB092iB10p10422.

Burgmann, R., G. Hilley, A. Ferretti, and F. Novali (2006), Resolving vertical tectonics in the San Francisco Bay Area from permanent scatterer InSAR and GPS analysis, *Geology*, *34*, 221–224.

Casu, F., M. Manzo, A. Pepe, and R. Lanari (2008), SBAS-DInSAR analysis of very extended areas: First results on a 60,000-km^2 test site, *IEEE Geosci. Remote Sens. Lett.*, *5*, 438–442.

Davis, J. L., B. P. Wernicke, S. Bisnath, N. A. Niemi, and P. Elosegui (2006), Subcontinental-scale crustal velocity changes along the Pacific-North American plate boundary, *Nature*, *441*, 1131–1134.

Dixon, T., F. Farina, C. DeMets, F. Suarez-Vidal, J. Fletcher, B. Marquez-Azua, M. Miller, O. Sanchez, and P. Umhoefer (2000a), New kinematic models for Pacific-North American motion from 3 Ma to present: II. Evidence for a "Baja California shear zone," *Geophys. Res. Lett.*, *27*, 3961–3964, doi:10.1029/2000GL008529.

Dixon, T. H., M. Miller, F. Farina, H. Z. Wang, and D. Johnson (2000b), Present-day motion of the Sierra Nevada block and some tectonic implications for the Basin and Range province, North American Cordillera, *Tectonics*, *19*, 1–24, doi:10.1029/1998TC001088.

Dixon, T. H., E. Norabuena, and L. Hotaling (2003), Paleoseismology and Global Positioning System: Earthquake-cycle effects and geodetic versus geologic fault slip rates in the eastern California shear zone, *Geology*, *31*(1), 55–58.

Dokka, R. K., and C. J. Travis (1990a), Late Cenozoic strike-slip faulting in the Mojave Desert, California, *Tectonics*, *9*, 311–340, doi:10.1029/TC009i002p00311.

Dokka, R. K., and C. J. Travis (1990b), Role of the eastern California shear zone in accommodating Pacific–North American plate motion, *Geophys. Res. Lett.*, *17*, 1323–1326, doi:10.1029/GL017i009p01323.

Feng, Q., and J. M. Lees (1998), Microseismicity, stress, and fracture in the Coso geothermal field, California, *Tectonophysics*, *289*, 221–238.

Ferretti, A., C. Prati, and F. Rocca (2001), Permanent scatterers in SAR interferometry, *IEEE Trans. Geosci. Remote Sens.*, *39*, 8–20.

Ferretti, A., M. Bianchi, C. Prati, and F. Rocca (2005), Higher-order permanent scatterers analysis, *EURASIP JASP*, *2005*, 3231–3242.

Fialko, Y. (2006), Interseismic strain accumulation and the earthquake potential on the southern San Andreas fault system, *Nature*, *441*, 968–971.

Gabriel, A. K., R. M. Goldstein, and H. A. Zebker (1989), Mapping small elevation changes over large areas – Differential radar interferometry, *J. Geophys. Res.*, *94*, 9183–9191, doi:10.1029/JB094iB07p09183.

Goldstein, R. M., H. Engelhardt, B. Kamb, and R. M. Frolich (1993), Satellite radar interferometry for monitoring ice-sheet motion - Application to an Antarctic ice stream, *Science*, *262*, 1525–1530.

Gourmelen, N. (2009), Measuring low fault strain rate with synthetic aperture radar interferometry: Application to the Pacific–North American plate boundary., PhD thesis, Univ. of Miami, Miami.

Gourmelen, N., and F. Amelung (2005), Postseismic mantle relaxation in the Central Nevada Seismic Belt, *Science*, *310*, 1473–1476.

Gourmelen, N., F. Amelung, F. Casu, M. Manzo, and R. Lanari (2007), Mining-related ground deformation in Crescent Valley, Nevada: Implications for sparse GPS networks, *Geophys. Res. Lett.*, *34*, L09309, doi:10.1029/2007GL029427.

Hanssen, R. (2001), *Radar Interferometry – Data Interpretation and Error Analysis*, Kluwer Academic Publishers, Dordrecht.

Hodges, K. V., L. W. Mckenna, J. Stock, J. Knapp, L. Page, K. Sternlof, D. Silverberg, G. Wust, and J. D. Walker (1989), Evolution of extensional basins and Basin and Range topography west of Death Valley, California, *Tectonics*, *8*(3), 453–467, doi:10.1029/TC008i003p00453.

Hooper, A., H. Zebker, P. Segall, and B. Kampes (2004), A new method for measuring deformation on volcanoes and other natural terrains using InSAR persistent scatterers, *Geophys. Res. Lett.*, *31*, L23611, doi:10.1029/2004GL021737.

Johnson, K. M., and P. Segall (2004), Viscoelastic earthquake cycle models with deep stress-driven creep along the San Andreas fault system, *J. Geophys. Res.*, *109*, B10403, doi:10.1029/2004JB003096.

Kohlhase, A. O., K. L. Feigl, and D. Massonnet (2003), Applying differential InSAR to orbital dynamics: a new approach for estimating ERS trajectories, *J. Geodesy*, *77*(9), 493–502.

Kreemer, C., G. Blewitt, and W. C. Hammond (2006), Using geodesy to explore correlations between crustal deformation characteristics and geothermal resources, p. 20, Geothermal Resources Council Annual Meeting, San Diego.

Lanari, R., O. Mora, M. Manunta, J. J. Mallorqui, P. Berardino, and E. Sansosti (2004), A small-baseline approach for investigating deformations on full-resolution differential SAR interferograms, *IEEE Trans. Geosci. Remote Sens.*, *42*, 1377–1386.

Lanari, R., F. Casu, M. Manzo, G. Zeni, P. Berardino, M. Manunta, and A. Pepe (2007), An overview of the small baseline subset algorithm: A DInSAR technique for surface deformation analysis, *Pure Appl. Geophys.*, *164*, 637–661.

Lee, J., D. F. Stockli, L. A. Owen, R. C. Finkel, and R. Kislitsyn (2009), Exhumation of the Inyo Mountains, California: Implications for the timing of extension along the western boundary of the Basin and Range Province and distribution of dextral fault slip rates across the eastern California shear zone, *Tectonics*, *28*, TC1001, doi:10.1029/2008TC002295.

Massonnet, D. (1997), Satellite radar interferometry, *Sci. Am.*, *276*, 46–53.

Massonnet, D., and K. L. Feigl (1998), Radar interferometry and its application to changes in the earth's surface, *Rev. Geophys.*, *36*, 441–500, doi:10.1029/97RG03139.

Massonnet, D., K. Feigl, M. Rossi, and F. Adragna (1994), Radar interferometric mapping of deformation in the year after the Landers earthquake, *Nature*, *369*, 227–230.

McClusky, S. C., S. C. Bjornstad, B. H. Hager, R. W. King, B. J. Meade, M. M. Miller, F. C. Monastero, and B. J. Souter (2001), Present day kinematics of the eastern California shear zone from a geodetically constrained block model, *Geophys. Res. Lett.*, *28*, 3369–3372, doi:10.1029/2000GL011851.

Meade, B. J., and B. H. Hager (2005), Block models of crustal motion in southern California constrained by GPS measurements, *J. Geophys. Res.*, *110*, B03403, doi:10.1029/2004JB003209.

Oswald, J. A., and S. G. Wesnousky (2002), Neotectonics and quaternary geology of the Hunter Mountain fault zone and Saline Valley region, southeastern California, *Geomorphology*, *42*(3), 255–278.

Peltzer, G., and P. Rosen (1995), Surface displacements of the 17 May 1993 Eureka Valley, California, earthquake observed by Sar interferometry, *Science*, *268*, 1333–1336.

Peltzer, G., F. Crampe, S. Hensley, and P. Rosen (2001), Transient strain accumulation and fault interaction in the eastern California shear zone, *Geology*, *29*, 975–978.

Pepe, A., and R. Lanari (2006), On the extension of the minimum cost flow algorithm for phase unwrapping of multitemporal differential SAR interferograms, *IEEE Trans. Geosci. Remote Sens.*, *44*, 2374–2383.

Pollitz, F. F., G. Peltzer, and R. Burgmann (2000), Mobility of continental mantle: Evidence from postseismic geodetic observations following the 1992 Landers earthquake, *J. Geophys. Res.*, *105*, 8035–8054, doi:10.1029/1999JB900380.

Rosen, P. A., S. Hensley, I. R. Joughin, F. K. Li, S. N. Madsen, E. Rodriguez, and R. M. Goldstein (2000), Synthetic aperture radar interferometry - Invited paper, *Proc. IEEE*, *88*, 333–382.

Rosen, P. A., S. Henley, G. Peltzer, and M. Simons (2004), Updated repeat orbit interferometry package released, *Eos Trans. AGU*, *85*.

Savage, J. C., and R. O. Burford (1973), Geodetic determination of relative plate motion in Central California, *J. Geophys. Res.*, *78*, 832–845, doi:10.1029/JB078i005p00832.

Savage, J. C., and M. Lisowski (1993), Inferred depth of creep on the Hayward fault, Central California, *J. Geophys. Res.*, *98*, 787–793, doi:10.1029/92JB01871.

Savage, J. C., and M. Lisowski (1998), Viscoelastic coupling model of the San Andreas fault along the big bend, southern California, *J. Geophys. Res.*, *103*, 7281–7292, doi:10.1029/98JB00148.

Scharroo, R. (2002), A Decade of ERS Satellite Orbits and Altimetry, Delft Univ. Technology, Netherlands.

Schmalzle, G. (2008), The Earthquake Cycle of Strike-Slip Faults, PhD thesis, Univ. of Miami, Miami.

Sibson, R. H. (1982), Fault zone models, heat-flow, and the depth distribution of earthquakes in the continental-crust of the United-States, *Bull. Seismol. Soc. Am.*, *72*, 151–163.

Sternloff, K. R. (1988), Structural Style and Kinematic History of the Active Panamint-Saline Extensional System, 30 pp., MIT., Inyo County, California.

Thatcher, W., and F. F. Pollitz (2008), Temporal evolution of continental lithospheric strength in actively deforming regions, *GSA Today*, *18*, 4–11.

Walter, A. W., and C. S. Weaver (1980), Seismicity of the Coso Range, California, *J. Geophys. Res.*, *85*, 2441–2458, doi:10.1029/JB085iB05p02441.

Weertman, J., and J. R. Weertman (1964), *Elementary Dislocation Theory*, 213 pp., Macmillan, New York.

Wernicke, B., A. M. Friedrich, N. A. Niemi, R. A. Bennett, and J. L. Davis (2000), Dynamics of plate boundary fault systems from Basin and Range Geodetic Network (BARGEN) and geological data, *GSA Today*, *10*, 1–7.

Wesnousky, S. G., and C. H. Jones (1994), Oblique slip, slip partitioning, spatial and temporal changes in the regional stress-field, and the relative strength of active faults in the Basin and Range, Western United States, *Geology*, *22*, 1031–1034.

Wicks, C. W., W. Thatcher, F. C. Monastero, and M. A. Hasting (2001), Steady state deformation of the Coso Range, east central California, inferred from satellite radar interferometry, *J. Geophys. Res.*, *106*, 13769–13780, doi:10.1029/2001JB000298.

Wright, T. J., B. Parsons, P. C. England, and E. J. Fielding (2004), InSAR observations of low slip rates on the major faults of western Tibet, *Science*, *305*, 236–239.

Zhang, P. Z., M. Ellis, D. B. Slemmons, and F. Y. Mao (1990), Right-lateral displacements and the holocene slip rate associated with prehistoric earthquakes along the southern Panamint Valley fault zone: Implications for southern Basin and Range tectonics and coastal California deformation, *J. Geophys. Res.*, *95*, 4857–4872, doi:10.1029/JB095iB04p04857.

F. Amelung, School of Marine and Atmospheric Science, University of Miami, 4600 Rickenbacker Causeway, Miami, FL 33149, USA.

N. Gourmelen, School of Earth and Environment, University of Leeds, Leeds, LS2 9JT UK. (n.gourmelen@leeds.ac.uk)

R. Lanari, Istituto per il Rilevamento Elettromagnetico dell'Ambiente, Via Diocleziano, 328, 8D124 Napoli, Italy.